Chemical Science

ROYAL SOCIETY OF CHEMISTRY

EDGE ARTICLE

View Article Online
View Journal | View Issue

Cite this: *Chem. Sci.*, 2023, **14**, 8962

All publication charges for this article have been paid for by the Royal Society of Chemistry

Electron delocalization of robust high-nuclear bismuth-oxo clusters for promoted CO_2 electroreduction†

Baoshan Hou,‡[a] Haiyan Zheng,‡[a] Kunhao Zhang,[c] Qi Wu,[a] Chao Qin,[a] Chunyi Sun,*[a] Qinhe Pan,[b] Zhenhui Kang,[d] Xinlong Wang*[ab] and Zhongmin Su[b]

The integration of high activity, selectivity and stability in one electrocatalyst is highly desirable for electrochemical CO_2 reduction (ECR), yet it is still a knotty issue. The unique electronic properties of high-nuclear clusters may bring about extraordinary catalytic performance; however, construction of a high-nuclear structure for ECR remains a challenging task. In this work, a family of calix[8]arene-protected bismuth-oxo clusters (BiOCs), including Bi_4 (**BiOC-1/2**), Bi_8Al (**BiOC-3**), Bi_{20} (**BiOC-4**), Bi_{24} (**BiOC-5**) and $Bi_{40}Mo_2$ (**BiOC-6**), were prepared and used as robust and efficient ECR catalysts. The $Bi_{40}Mo_2$ cluster in **BiOC-6** is the largest metal-oxo cluster encapsulated by calix[8]arenes. As an electrocatalyst, **BiOC-5** exhibited outstanding electrochemical stability and 97% Faraday efficiency for formate production at a low potential of −0.95 V *vs.* RHE, together with a high turnover frequency of up to 405.7 h^{-1}. Theoretical calculations reveal that large-scale electron delocalization of BiOCs is achieved, which promotes structural stability and effectively decreases the energy barrier of rate-determining *OCHO generation. This work provides a new perspective for the design of stable high-nuclear clusters for efficient electrocatalytic CO_2 conversion.

Received 8th June 2023
Accepted 31st July 2023

DOI: 10.1039/d3sc02924g

rsc.li/chemical-science

Introduction

Electrochemical CO_2 reduction (ECR) has been considered as a promising technology to achieve a carbon-neutral cycle.[1,2] ECR is characterized by multielectron and proton transfer[3–6] *via* multiple pathways, which leads to a variety of reduction products;[7] therefore, the activity, selectivity and stability of electrocatalysts are crucial to the development of ECR. To comprehensively optimize the catalytic reactivity and selectivity, various strategies have been explored, such as heteroatom doping,[8] alloy/dealloying,[9] oxidation state adjustment,[10] and organic moiety control,[11] with the prevailing model locally at individual active sites.[12,13] Recently, the effect of electron delocalization on electrocatalytic activity has attracted increasing attention, by which the energetic barriers of key intermediates could be modulated.[14,15] Moreover, the additional charge (lost or gained) could uniformly distribute over all atoms, and the stability of catalysts during the electrochemical process may be increased which will help to solve the intractable dynamic reconstruction issue of electrocatalysts.[16–18] Clusters are atomic-precision architectures located between atoms and nanomaterials.[19] The electronic properties of some clusters have been exhibited to resemble those of atoms,[20–23] and thus, large-scale electron delocalization may appear in clusters,[24] yet, related research on catalysis is in its infancy. High-nuclear clusters are famous for their high surface-atom ratio, which could supply abundant metal active species for electrocatalysis.[25,26] However, the construction of stable high-nuclear clusters with ECR activity is still a huge challenge.[27,28]

Over the past decades, Bi-based materials have been extensively investigated as electrocatalysts because of their activity toward high-valued HCOOH production.[29–34] In this work, we chose *t*-butylcalix[8]arene (TBC[8]) as a ligand to assemble with Bi^{3+}, achieving unprecedented high-nuclear Bi-oxo clusters (BiOCs).[35,36] Controlled hydrolysis of Bi^{3+} ions to promote crystallization is a basic prerequisite for obtaining high-nuclear BiOCs.[37,38] Chelating organoamine with weakly coordinated N-

---

[a] *Key Lab of Polyoxometalate Science of Ministry of Education, National & Local United Engineering Laboratory for Power Battery Institution, Northeast Normal University, Changchun, Jilin, 130024, China. E-mail: wangxl824@nenu.edu.cn; suncy009@nenu.edu.cn*

[b] *Key Laboratory of Advanced Materials of Tropical Island Resources, Ministry of Education, Hainan University, Haikou, 570228, China*

[c] *Shanghai Synchrotron Radiation Facility, 239 Zhangheng Road, Pudong New District, Shanghai, 200120, China*

[d] *Institute of Functional Nano & Soft Materials, Jiangsu Key Laboratory for Carbon-Based Functional Materials & Devices, Soochow University, Suzhou 215123, Jiangsu, China*

† Electronic supplementary information (ESI) available. CCDC 2236082–2236087. For ESI and crystallographic data in CIF or other electronic format see DOI: https://doi.org/10.1039/d3sc02924g

‡ These authors contributed equally to this work.

donors, such as ethylenediamine (en), can exert a slow release effect on oxophilic Bi^{3+} ions through coordination (*i.e.*, providing low concentrations of Bi^{3+} ions), thus avoiding rapid precipitation.[39,40] Besides, the hydrolysis-limited ligands with strong coordination ability can delay the hydrolysis of Bi^{3+} ions.[41,42] In addition, the introduction of second metal ions into BiOCs is another effective strategy to achieve a deep self-assembly to form high-nuclear BiOCs.[43,44] As a macrocyclic octamer of phenols, TBC[8] can simultaneously grab more Bi^{3+} ions through multiple pre-organized phenoxy (hydroxyl) sites and delay the hydrolysis of Bi^{3+}. Meanwhile, the continuous carbon backbone of TBC[8] can further provide an additional stabilization effect for BiOCs.

Herein, a family of calix[8]arene-protected bismuth-oxo clusters, including 4-nuclear Bi_4 (**BiOC-1/2**), 9-nuclear Bi_8Al (**BiOC-3**), 20-nuclear Bi_{20} (**BiOC-4**), 24-nuclear Bi_{24} (**BiOC-5**) and 42-nuclear $Bi_{40}Mo_2$ (**BiOC-6**), were successfully assembled from TBC[8] and Bi^{3+} ions under solvothermal conditions. The $Bi_{40}Mo_2$ in **BiOC-6** is the largest calix[8]arene-based metal-oxo cluster reported so far. The properties of the solvents had a great influence on the assembly of these Bi–O clusters. The pure methanol environment produced only small-sized Bi_4 clusters. Meanwhile the introduction of DMF significantly increased the nuclearity of Bi_8Al and Bi_{20}. Increasing the ratio of methanol in methanol/DMF ultimately gave rise to high-nuclear Bi_{24} and the largest $Bi_{40}Mo_2$. As ECR catalysts, such BiOCs exhibit high structural stability, outstanding turnover frequency (TOF) and extraordinary Faraday efficiency (FE) towards HCOOH generation over a wide potential range. It is noteworthy that the FE_{HCOOH} of **BiOC-5** reaches 97% at −0.95 V, which is 16% higher than that of **BiOC-4**. The analysis of the electron gain and loss process by DFT calculations indicates that a nuclear-related electron-delocalization effect is achieved in these BiOCs. Catalytic mechanism studies verify that *OCHO is a key intermediate for HCOOH formation and electron delocalization plays an essential role in lowering the free energy of the *OCHO production step.

Results and discussion

A family of TBC[8]-protected bismuth-oxo clusters with different nuclearities were constructed by varying the type of solvent or introducing second metal ions using $Bi(NO_3)_3$ and TBC[8] with the assistance of organic amines. When the solvent was CH_3OH, only two 4-nuclear **BiOC-1** (Bi_4) and **BiOC-2** (Bi_4) were obtained. Meanwhile **BiOC-4** (Bi_{20}) and **BiOC-5** (Bi_{24}) with higher nucleation were formed after the introduction of DMF into the reaction system, indicating that the solvent has an important influence on the nucleation process of BiOCs. In addition, the availability of the heterometallic clusters **BiOC-3** (Bi_8Al) and **BiOC-6** ($Bi_{40}Mo_2$) indicates that BiOCs are quite compatible with other metal ions and the introduction of heterometallic clusters is beneficial for structural modulation (Fig. 1, S1 and Table S1†). Meanwhile, the flexible coordination mode of the TBC[8] ligand is another important factor for the structural diversity of BiOCs. A total of 10 different coordination modes of TBC[8]–Bi were found in the structures of **BiOC-1** to **6** (Fig. S2†). The eight phenolic hydroxyl groups of the TBC[8] ligands can simultaneously coordinate with 4–8 Bi ions and exhibit flexible and diverse coordination patterns. One of the most typical patterns is TBC[8]–Bi_4 (Fig. S2b†), where the four central phenolic hydroxyl groups are coordinated with two Bi ions *via* the μ_2–η^1:η^1 form, while the other four marginal phenolic hydroxyl groups are coordinated to one Bi ion with Bi–Bi distances of approximately 3.67 Å and 3.69 Å. It is worth mentioning that the coordination pattern of TBC[8]–Bi_8 found in **BiOC-6** is very rare among TBC[8] complexes (Fig. S2j†) and can be described as the four marginal phenolic hydroxyl groups

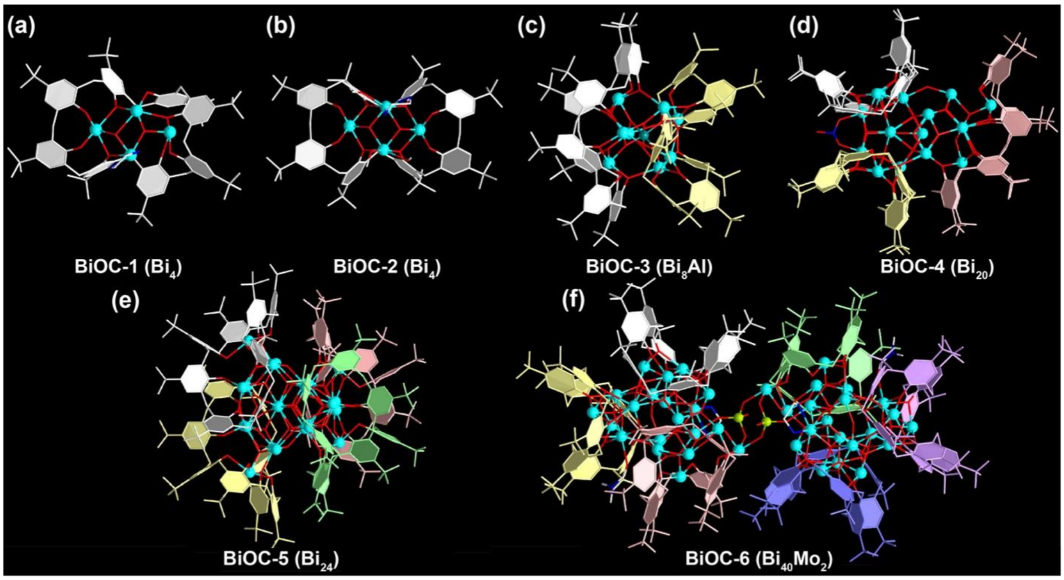

Fig. 1 The crystal structures of BiOC-1 (a), BiOC-2 (b), BiOC-3 (c), BiOC-4 (d), BiOC-5 (e), and BiOC-6 (f). Atom color code: sky blue: Bi; red: O; white: C; blue: N; light green: Mo; teal: Al.

in TBC[8]–Bi_4 also adopt the μ_2–η^1:η^1 form to coordinate with other four Bi ions. These results indicate the promise of enriching the structural diversity of BiOCs by modulating the appropriate reaction conditions and the coordination pattern of TBC[8] ligands.

To better understand the structures of this family of BiOCs, we describe them in terms of different degrees of aggregation of TBC[8]. **BiOC-1** and **BiOC-2** represent the two structurally simplest TBC[8]–Bi_4 isomeric monomers, in which each Bi_4 cluster is bridged to a TBC[8] ligand on one side, and the rest of the coordination sites are occupied by ethylenediamine or methanol (Fig. 1a, b, and S3†). The different distortion angles of TBC[8] lead to structural variations.[45] Meanwhile, the structure of **BiOC-3** (Bi_8Al) is a TBC[8]–Bi_4 dimer interconnected by the central Al^{3+} ion in which two TBC[8] ligands are located on the pole positions (Fig. 1c). If more TBC[8] ligands are introduced on the BiOCs surface, larger metal-oxo clusters need to be formed to reduce the steric hindrance between the organic ligands. The structure of **BiOC-4** (Bi_{20}) confirms that the smallest cluster constructing the TBC[8] trimer is Bi_{20}, and three TBC[8] ligands are uniformly distributed on the surface (Fig. 1d). The tetramer **BiOC-5** (Bi_{24}) is composed of four TBC[8]–Bi_5 subunits wrapped around the middle Bi_4 cluster with a tetrahedral conformation (Fig. 1e). **BiOC-6** ($Bi_{40}Mo_2$) is the largest metal-oxo cluster encapsulated by the TBC[8] ligand, which is composed of two Bi_{20} clusters bridged by two $\{MoO_4\}$ tetrahedra (Fig. 1f and S4†). Structural analysis of **BiOC-1–6** confirms that TBC[8] is a compatible macrocyclic ligand for building high-nuclear metal-oxo clusters with strong metal ion trapping ability and flexible coordination modes.

To explore the feasibility of high-nuclear BiOCs as CO_2 reduction electrocatalysts, **BiOC-4** and **BiOC-5** were selected as electrocatalysts due to their high yields. Chemical stability studies show that both of them can retain their crystallinity under ambient conditions and in aqueous solutions at pH = 0.3–14, as confirmed by PXRD patterns (Fig. S12–S15†). The ECR electrocatalytic activity and selectivity of **BiOC-4** and **BiOC-5** are evaluated in a two-compartment gas-tight electrochemical H-type cell. Their linear cyclic voltammetry (LSV) curves are recorded under CO_2-saturated (pH = 7.4) and N_2-saturated (pH = 8.7) 0.5 M $KHCO_3$ solutions (Fig. 2a) to preliminary characterize their activity. Both of them demonstrate a higher current density and more positive onset potential in the CO_2-saturated electrolyte compared with N_2-saturated conditions, which verifies that ECR is preferred to the competitive HER at the cathode. The cathodic current density of **BiOC-5** abruptly takes off at ∼−0.8 V and reaches a total current density of 28.1 mA cm^{-2} at −1.1 V. Meanwhile, **BiOC-5** demonstrates a larger cathodic current density than **BiOC-4** (16.3 mA cm^{-2}), suggesting that **BiOC-5** has favorable activity for ECR.

The electrocatalytic ECR selectivity of **BiOC-4** and **BiOC-5** was biased in the selected potential range (−0.8 to −1.1 V) (Fig. S16 and S17†). The gaseous and liquid products were quantitatively analyzed by gas chromatography (GC) and ion chromatography (IC) after one-hour electrolysis. Fig. 2b illustrates that HCOOH is the major liquid product over the applied potential range from −0.8 to −1.1 V, and CO and H_2 were minor gaseous products. To illuminate the origination of the product, control experiments under N_2-saturated conditions were performed. No carbon-reduction product (CO and HCOOH) is found by GC and IC, verifying that the carbon-reduction products result from CO_2 reduction. To be more credible, the ^1H NMR spectrum was employed to check the liquid product and the results are consistent with that of IC analysis (Fig. S18†). Under CO_2-saturated conditions, **BiOC-5** maintains a high FE of over 92% in a large potential window between −0.9 and −1.1 V and reaches a maximum of 97% at −0.95 V. In contrast, the maximum FE_{HCOOH} over **BiOC-4** is less than 82%. The FE_{HCOOH} of **BiOC-5** is not only superior to that of **BiOC-4** but also ranks among the best activity values of Bi-based ECR catalysts (Fig. 2e and Table S2†). The corresponding FE_{H2} and FE_{CO} are depicted in Fig. S19 and S20.† Then, the partial current density of formate (j_{HCOOH}) for both **BiOC-4** and **BiOC-5** was calculated. **BiOC-5** presents a larger j_{HCOOH} of 22.6 mA cm^{-2}, almost twice that of **BiOC-4** (11.7 mA cm^{-2}).

To estimate the electrocatalytic reactivity of **BiOC-4** and **BiOC-5**, the electrochemically active surface area (ECSA) is analyzed, firstly. From the values of electrochemical double-layer capacitance (C_{dl}) based on cyclic voltammetry (CV) curves, we can find that **BiOC-5** has a larger C_{dl} than **BiOC-4**, suggesting that **BiOC-5** can provide more available active sites for contact with the ECR electrolyte (Fig. S21†). This provides a prerequisite for the high catalytic activity of **BiOC-5**. Next, the turn-around frequency (TOF) was calculated (for calculation details, please see the ESI†). **BiOC-4** presents a TOF of 276.59 h^{-1} for HCOOH formation at −1.1 V, while **BiOC-5** shows an impressive reaction rate with a TOF of 405.7 h^{-1} at −1.1 V, which outperforms the performance of crystalline Bi-based electrocatalysts.[46,47] Catalytic durability is one of the crucial parameters for evaluating the application potential of electrocatalysts. Therefore, a long-time electrolysis experiment was performed at a potential of −0.95 V. The current curve illustrates that **BiOC-5** can keep the current density roughly unchanged in a 24 h reaction (Fig. 2d). It worth noting that the FE_{HCOOH} of **BiOC-5** still remains at higher than 95% over this reaction period. These results unambiguously demonstrate that **BiOC-5** is a robust electrocatalyst for ECR.

The reaction kinetics for HCOOH production are studied. **BiOC-5** exhibits a relatively lower Tafel slope of 220 mV dec^{-1} compared to **BiOC-4** (260 mV dec^{-1}), evidencing the favorable kinetics of **BiOC-5** for ECR (Fig. 2c). Again, this means that the initial electron transfer for the formation of the *OCHO intermediate on the catalyst surface is the rate-determining step. Furthermore, electrochemical impedance (EIS) was performed for both catalysts at −0.95 V (Fig. S22†). According to the results of the Nyquist plots, **BiOC-5** possesses a much smaller semicircle diameter, reflecting faster electron transfer efficiency.

Since Bi-based materials often undergo dynamic reconstruction during ECR, to determine whether the structure of BiOCs is maintained, X-ray absorption near edge structure (XANES) and extended X-ray absorption fine structure (EXAFS) spectroscopy were performed, taking **BiOC-5** as an example.

Both the absorption edge and white line peak of the XANES spectrum for **BiOC-5** nearly overlap with that of the Bi_2O_3

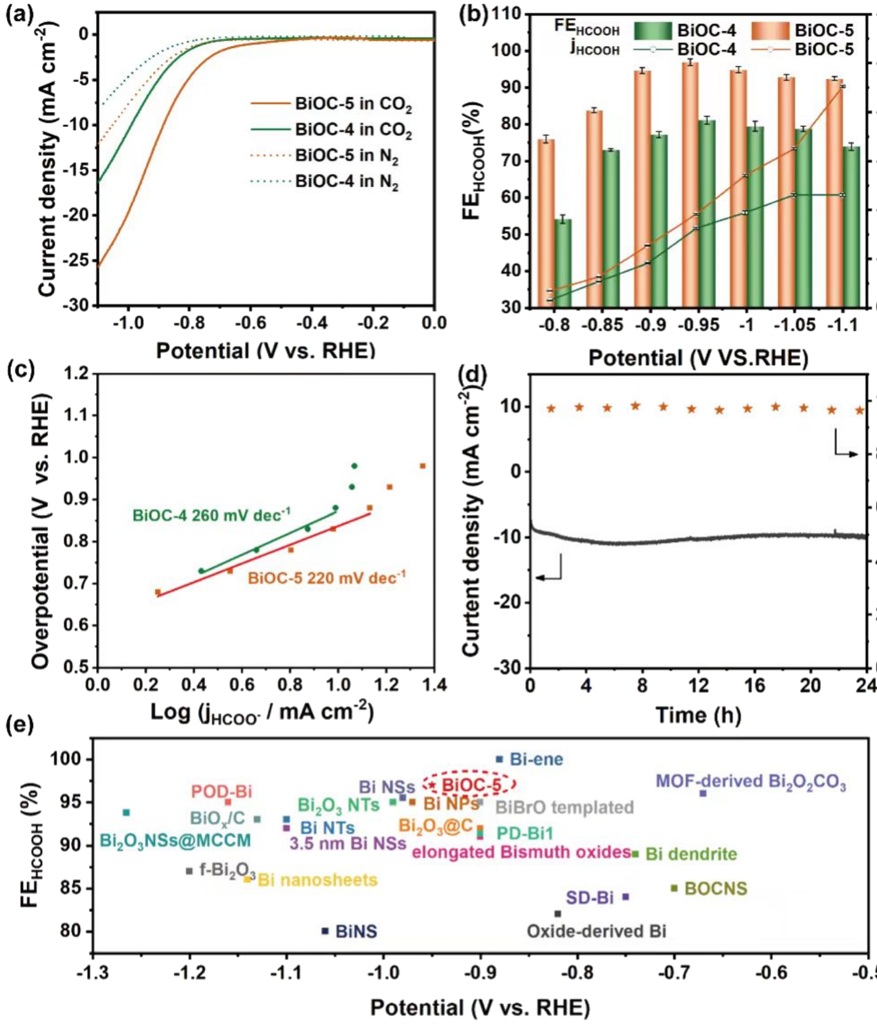

Fig. 2 (a) Polarization curves of BiOC-4 and BiOC-5 in N_2 or CO_2 saturated 0.5 M $KHCO_3$. (b) Faradaic efficiencies of production and the current densities of formate at different working potentials in a CO_2-saturated 0.5 M $KHCO_3$ electrolyte for BiOC-4 and BiOC-5. (c) Nyquist plots for BiOC-4 and BiOC-5. (d) Stability test of BiOC-5 at −0.95 V *vs.* RHE for 24 h. (e) Comparison of FE_{HCOOH} with previously documented reports.

reference, suggesting that Bi atoms in **BiOC-5** are Bi^{3+} species (Fig. 3a). After ECR, the absorption edge of **BiOC-5** only slightly shifts toward lower energy, indicating that the oxidation state of Bi is mainly retained. By fitting the recorded spectrum with the window from 1 to 6 Å, we obtained the bond lengths of Bi foil, Bi_2O_3, **BiOC-5** before and **BiOC-5** after catalysis (Fig. 3b).[48] The EXAFS curves of the Bi L3-edge reveal the main peak at 1.6 Å, corresponding to the scattering path of the Bi–O bond. The Bi–Bi oscillation of metallic–Bi at 3.3 Å was not observed during the long-term electrochemical process, which illuminates the robust chemical stability of **BiOC-5** during ECR.[15]

Besides, a series of spectral analyses were performed to further reveal the structural stability during ECR. The PXRD pattern and FT-IR spectrum of the electrocatalysts after stability testing were almost identical to before catalysis, indicating that **BiOC-4** and **BiOC-5** can maintain their structural integrity during ECR (Fig. S23–S26†). XPS spectral analysis did not detect Bi^0 before and after the ECR experiment, and the oxidized state of Bi was well preserved (Fig. S27†). The *in situ* Raman spectrum provides persuasive evidence that the structure of BiOCs can be preserved as expected (Fig. 3c). Furthermore, the morphology of the BiOC catalyst is largely preserved as shown by SEM images (Fig. S28†). In a word, all the above results demonstrated that BiOCs possess extraordinary stability toward ECR.

In situ FTIR measurements were conducted to identify the intermediates during the ECR process. As illustrated in Fig. 3d, the peaks appear at 1326, 1438, 1479 and 1531 cm^{-1} attributed to the stretching vibration of m-CO_3^{2-}, and at 1278 and 1552 cm^{-1} belonging to the stretching vibration of b-CO_3^{2-}.[49] The bands at 1409 and 1662 cm^{-1} in the spectra are attributed to HCO_3^-.[49] Most importantly, the *OCHO intermediate signals detected at 1380 and 1591 cm^{-1} are generally regarded as key intermediates in the electrochemical $CO_2 \rightarrow HCOOH$ conversion and increase gradually with the applied potentials varying between −0.7 and −1.5 V.[50] Besides, the characteristic peaks of $HCOO^-$ (1629, 1689, 1727, 1760, and 1785 cm^{-1}) start to appear with increasing voltage.[51]

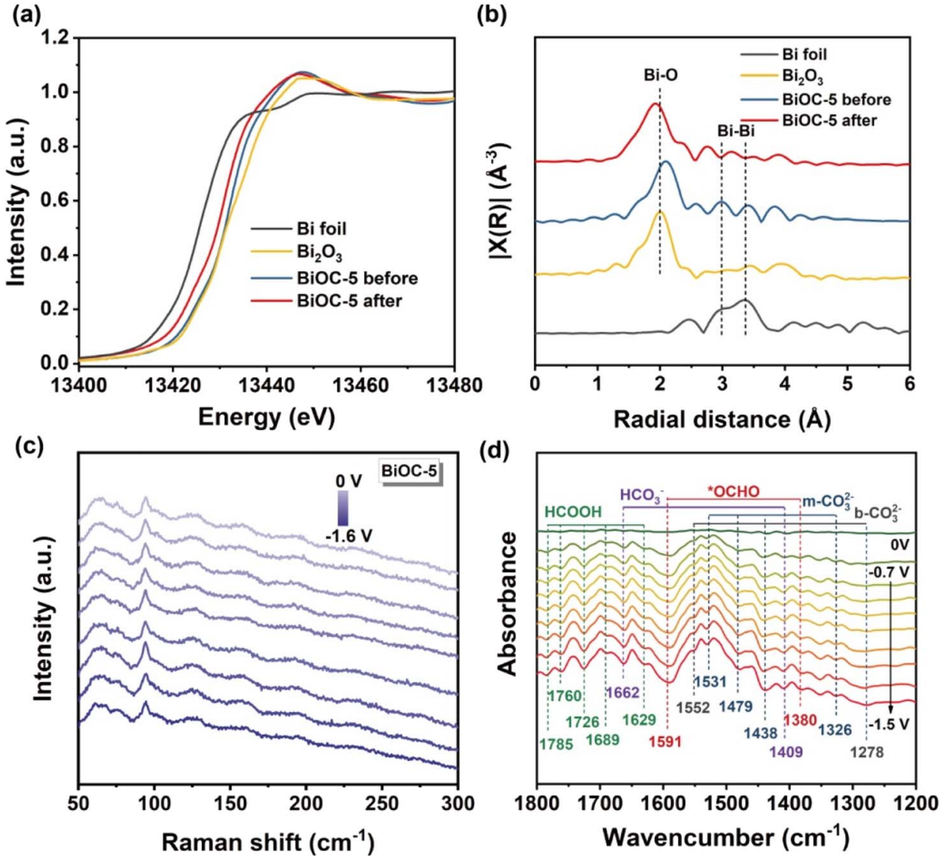

Fig. 3 (a) Bi L3-edge XANES spectra of Bi foil, Bi_2O_3, **BiOC-5** before and **BiOC-5** after. (b) EXAFS in R-space for Bi foil, Bi_2O_3, **BiOC-5** before and **BiOC-5** after. (c). *In situ* Raman spectra of CO_2 reduction on **BiOC-5**. (d) *In situ* ATR-FTIR spectra of **BiOC-5** during the ECR.

To gain a deep understanding of the high stability and the outstanding catalytic activity and selectivity of BiOC catalysts, theoretical calculations were performed. The charge distribution on the LUMO orbital and the localized orbital locator (LOL) maps suggest that significant electron delocalization occurs throughout the BiOC clusters (Fig. S29 and S30†). The orbital delocalization index (ODI) of LUMO orbitals is a significant factor to evaluate the extent of spatial delocalization. The small ODI value of **BiOC-5** in contrast to **BiOC-4** (1.56 *vs.* 5.58) indicates that **BiOC-5** possesses a much wider range of electron delocalization. These results are further corroborated by the projected density of states (PDOS) of all Bi atoms in **BiOC-4** and **BiOC-5** (Fig. 4a and b). The roughly equivalent contributions of each Bi atom on the non-occupied orbitals demonstrate that each Bi atom could accept additional electrons. Compared to **BiOC-4**, the PDOS of **BiOC-5** is closer to the Fermi energy level, which indicates a stronger electron-donating capability for **BiOC-5**, while the narrower band gap provides a better electron transport capability. Furthermore, the vertical ionization energy was calculated for **BiOC-4** and **BiOC-5**, the charge of which is neutralized by protons (Table S3†).[24] The results present that **BiOC-4** needs 156.112 kcal mol^{-1} to ionize the first electron, which is larger than 79.759 kcal mol^{-1} required by **BiOC-5**. Therefore, we speculate that electron delocalization is achieved in such metal-oxo clusters, which enables the entire cluster to act as an active catalytic site and may facilitate the catalytic process. The electron delocalization on the metal-oxo cluster also contributes to the structural stability in the electrocatalytic CO_2RR process.[52,53]

The reaction energy pathways for CO_2 reduction to HCOOH and the competing hydrogen evolution reaction were explored by density functional theory (DFT) calculations. Both **BiOC-4** and **BiOC-5** have lower energy barriers for *OCHO formation than for H* formation (Fig. S31†). Therefore, HCOOH production is preferential on **BiOC-4** and **BiOC-5**. Moreover, the hydrophobic skeleton of **BiOC-4** and **BiOC-5** (contact angle in Fig. S32†) also helps to suppress hydrogen production. Fig. 4c illustrates the optimized structures and energies of the CO_2RR pathway involved in each dominant intermediate. For **BiOC-5**, the Gibbs free energy change (ΔG) of *OCHO formation is calculated to be +0.54 eV, whereas the ΔG for **BiOC-4** is +0.62 eV. It implies that this step is thermodynamically more favorable on **BiOC-5**. Subsequently, these intermediates accept electrons and protons to form adsorbed HCOOH and desorb from the catalyst surface. Furthermore, the maximum energy barriers of **BiOC-5** are observed for *OCHO formation, indicating that the first electron/proton transfer was the chemical rate-determining step. Moreover, **BiOC-5** shows a great ΔG for *H formation, which could inhibit the generation of H_2 compared with **BiOC-4**. It's conjectured that the electron delocalization effect possibly has an essential contribution in lowering the energy barrier to the formation of *OCHO intermediates in the CO_2RR.

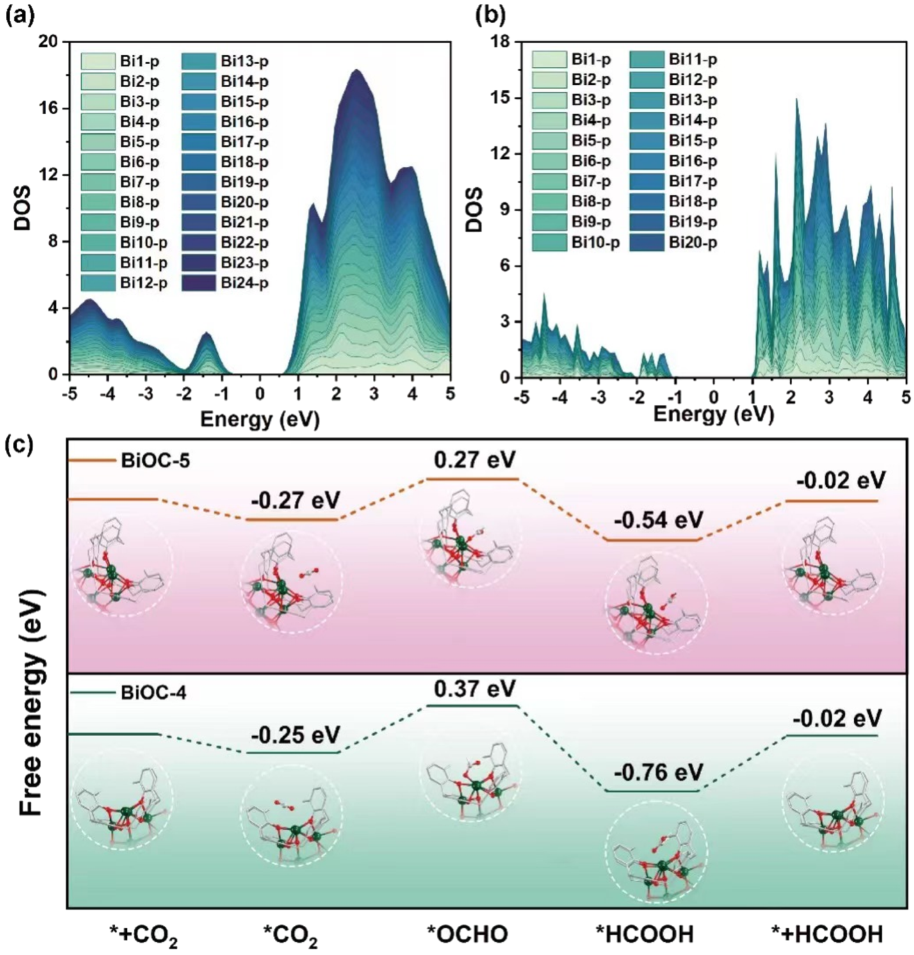

Fig. 4 (a and b) PDOS of all Bi atoms for **BiOC-4** and **BiOC-5**. (c) Free-energy diagrams for HCOOH on **BiOC-4** and **BiOC-5**.

Besides, 4-core **BiOC-1** was further selected to be analyzed and evaluated for ECR to confirm the results and conclusions (Fig. S33†). The results are as predicted where less core-numbered **BiOC-1** exhibits the smallest FE_{HCOOH} of 75% and j_{HCOOH} of −9.63 mA cm^{-2} compared to **BiOC-4** and **BiCO-5**, implying the rationality of the conclusions.

Conclusions

In summary, a family of calix[8]arene-protected bismuth-oxo clusters with robust stability were synthesized and explored as catalysts for the electrochemical reduction of CO_2 to HCOOH. Calix[8]arene is proved to be an excellent macrocyclic ligand for the construction of high-nuclear metal-oxo clusters with its strong ion-trapping ability and flexible coordination modes. The $Bi_{40}Mo_2$ cluster in **BiOC-6** is the first metal-oxo cluster with more than 40 metal centers constructed from calix[8]arenes, illuminating significant progress in the synthesis of calix[8]arene-based high-nuclear clusters. Notably, BiOCs present excellent stability during an electrocatalytic process, and **BiOC-5** achieves high selectivity for formate production over a wide potential range with an outstanding maximum Faraday efficiency of 97% at −0.95 V *vs.* RHE. Besides, **BiOC-5** achieves an impressive TOF of 405.7 h^{-1}, ranking among the highest values of crystalline Bi-based materials. Overall, **BiOC-5** exhibits high catalytic selectivity and activity, while maintaining high structural stability for ECR. DFT calculations suggest that electron delocalization occurs in **BiOC-5**, resulting in the uniform distribution of additional charge on all Bi atoms and low energy for electron departure. This not only guarantees structural stability, but also reliably improves the conversion efficiency of CO_2 to HCOOH by decreasing the ΔG of decisive *OCHO formation. This study not only paves the way for the construction of high-nuclear metal-oxo clusters but also illustrates the superiority of clusters as catalysts for CO_2 electroreduction.

Data availability

All experimental supporting data and procedures are available in the ESI.†

Author contributions

C. Y. S. and X. L. W. conceived the idea and designed the experiments. B. S. H. performed the SCXRD measurement and crystal structure analysis. H. Y. Z. performed the electrochemical studies. Q. W. performed the DFT calculations. K. H. Z. performed the single-crystal synchrotron X-ray diffraction measurements. Z. H. K., Q. H. P and Z. M. S. contributed to the general methodology and assisted with data interpretation. C. Q., C. Y. S. and X. L. W. co-drafted the manuscript and reviewed/revised the manuscript. All authors contributed to the analysis of the manuscript.

Conflicts of interest

The authors declare no competing interests.

Acknowledgements

This work was financially supported by the NSFC of China (No. 21971032), Foundation of Jilin Educational Committee (No. JJKH20221153KJ), and Jilin Provincial Department of Science and Technology (No. 20230508108RC).

References

1 L. L. Zhuo, P. Chen, K. Zheng, X. W. Zhang, J. X. Wu, D. Y. Lin, S. Y. Liu, Z. S. Wang, J. Y. Liu, D. D. Zhou and J. P. Zhang, *Angew. Chem., Int. Ed.*, 2022, **61**, e202204967.

2 S. Navarro-Jaén, M. Virginie, J. Bonin, M. Robert, R. Wojcieszak and A. Y. Khodakov, *Nat. Rev. Chem.*, 2021, **5**, 564–579.

3 G. B. Wen, B. H. Ren, Y. Zheng, M. Li, C. Silva, S. Q. Song, Z. Zhang, H. Z. Dou, L. Zhao, D. Luo, A. P. Yu and Z. W. Chen, *Adv. Energy Mater.*, 2022, **12**, 2103289.

4 W. Zhang, C. Q. Huang, J. X. Zhu, Q. C. Zhou, R. H. Yu, Y. L. Wang, P. F. An, J. Zhang, M. Qiu, L. Zhou, L. Q. Mai, Z. G. Yi and Y. Yu, *Angew. Chem., Int. Ed.*, 2022, **61**, e202112116.

5 S. Nitopi, E. Bertheussen, S. B. Scott, X. Y. Liu, A. K. Engstfeld, S. Horch, B. Seger, I. E. L. Stephens, K. Chan, C. Hahn, J. K. Nørskov, T. F. Jaramillo and I. Chorkendorff, *Chem. Rev.*, 2019, **119**, 7610–7672.

6 Q. Zhao, J. M. P. Martirez and E. A. Carter, *J. Am. Chem. Soc.*, 2021, **143**, 6152–6164.

7 Y. H. Wang, Z. Y. Wang, C. T. Dinh, J. Li, A. Ozden, M. G. Kibria, A. Seifitokaldani, C. S. Tan, C. M. Gabardo, M. C. Luo, H. Zhou, F. W. Li, Y. W. Lum, C. McCallum, Y. Xu, M. X. Liu, A. Proppe, A. Johnston, P. Todorovic, T. T. Zhuang, D. Sinton, S. O. Kelley and E. H. Sargent, *Nat. Catal.*, 2019, **3**, 98.

8 Y. S. Zhou, F. L. Che, M. Liu, C. Q. Zou, Z. Q. Liang, P. D. Luna, H. F. Yuan, J. Li, Z. Q. Wang, H. P. Xie, H. M. Li, P. N. Chen, E. Bladt, R. Quintero-Bermudez, T. K. Sham, S. Bals, J. Hofkens, D. Sinton, G. Chen and E. H. Sargent, *Nat. Chem.*, 2018, **10**, 974–980.

9 E. L. Clark, C. Hahn, T. F. Jaramillo and A. T. Bell, *J. Am. Chem. Soc.*, 2017, **139**, 15848–15857.

10 P. D. Luna, R. Quintero-Bermudez, C. T. Dinh, M. B. Ross, O. S. Bushuyev, P. Todorović, T. Regier, S. O. Kelley, P. D. Yang and E. H. Sargent, *Nat. Catal.*, 2018, **1**, 103–110.

11 M. S. Xie, B. Y. Xia, Y. W. Li, Y. Yan, Y. H. Yang, Q. Sun, S. H. Chan, A. Fishere and X. Wang, *Energy Environ. Sci.*, 2016, **9**, 1687–1695.

12 Z. W. Huang, J. X. Liang, D. M. Tang, Y. X. Chen, W. Y. Qu, X. L. Hu, J. X. Chen, Y. Y. Dong, D. R. Xu, D. Golberg, J. Li and X. F. Tang, *Chem*, 2022, **8**, 3008–3017.

13 S. Nitopi, E. Bertheussen, S. B. Scott, X. Y. Liu, A. K. Engstfeld, S. Horch, B. Seger, I. E. L. Stephens, K. Chan, C. Hahn, J. K. Nørskov, T. F. Jaramillo and I. Chorkendorff, *Chem. Rev.*, 2019, **119**, 7610–7672.

14 H. Sun, L. Chen, L. K. Xiong, K. Feng, Y. F. Chen, X. Zhang, X. Z. Yuan, B. Y. Yang, Z. Deng, Y. Liu, M. H. Rümmeli, J. Zhong, Y. Jiao and Y. Peng, *Nat. Commun.*, 2021, **12**, 6823.

15 S. S. He, F. L. Ni, Y. J. Ji, L. Wang, Y. Z. Wen, H. P. Bai, G. J. Liu, Y. Zhang, Y. Y. Li, B. Zhang and H. S. Peng, *Angew. Chem., Int. Ed.*, 2018, **57**, 16114–16119.

16 C. S. Cao, D. D. Ma, J. F. Gu, X. Y. Xie, G. Zeng, X. F. Li, S. G. Han, Q. L. Zhu, X. T. Wu and Q. Xu, *Angew. Chem., Int. Ed.*, 2020, **59**, 15014–15020.

17 D. Z. Yao, C. Tang, A. Vasileff, X. Zhi, Y. Jiao and S. Z. Qiao, *Angew. Chem., Int. Ed.*, 2021, **60**, 18178–18184.

18 J. Y. Duan, T. Y. Liu, Y. H. Zhao, R. O. Yang, Y. Zhao, W. B. Wang, Y. W. Liu, H. Q. Li, Y. F. Li and T. Y. Zhai, *Nat. Commun.*, 2022, **13**, 2039–2049.

19 Q. D. Liu and X. Wang, *Chem Catal.*, 2022, **2**, 1257–1266.

20 S. N. Khanna and P. Jena, *Phys. Rev. B: Condens. Matter Mater. Phys.*, 1995, **51**, 13705–13716.

21 C. Bo and J. M. Poblet, *Isr. J. Chem.*, 2011, **51**, 228–237.

22 Q. Tang, G. X. Hu, V. Fung and D. E. Jiang, *Acc. Chem. Res.*, 2018, **51**, 2793–2802.

23 L. R. Liu, P. Li, L. F. Yuan, L. J. Cheng and J. L. Yang, *Nanoscale*, 2016, **8**, 12787–12792.

24 Q. D. Liu, Q. H. Zhang, W. X. Shi, H. S. Hu, J. Zhuang and X. Wang, *Nat. Chem.*, 2022, **14**, 433–440.

25 B. W. J. Chen, L. Xu and M. Mavrikakis, *Chem. Rev.*, 2021, **121**, 1007–1048.

26 Y. Liu, N. O. Weiss, X. D. Duan, H. C. Cheng, Y. Huang and X. F. Duan, *Nat. Rev. Mater.*, 2016, **1**, 16042.

27 W. H. Fang, L. Zhang and J. Zhang, *J. Am. Chem. Soc.*, 2016, **138**, 7480–7483.

28 M. X. Ma, X. L. Ma, G. M. Liang, X. T. Shen, Q. L. Ni, L. C. Gui, X. J. Wang, S. Y. Huang and S. M. Li, *J. Am. Chem. Soc.*, 2021, **143**, 13731–13737.

29 N. Han, Y. Wang, H. Yang, J. Deng, J. H. Wu, Y. F. Li and Y. G. Li, *Nat. Commun.*, 2018, **9**, 1320–1327.

30 F. P. G. D. Arquer, O. S. Bushuyev, P. D. Luna, C. T. Dinh, A. Seifitokaldani, M. I. Saidaminov, C. S. Tan, L. N. Quan, A. Proppe, M. G. Kibria, S. O. Kelley, D. Sinton and E. H. Sargent, *Adv. Mater.*, 2018, **30**, 1802858.

31 H. Yang, N. Han, J. Deng, J. H. Wu, Y. Wang, Y. P. Hu, P. Ding, Y. F. Li, Y. G. Li and J. Lu, *Adv. Energy Mater.*, 2018, **8**, 1801536.

32 Y. Zhang, X. L. Zhang, Y. Z. Ling, F. W. Li, A. M. Bond and J. Zhang, *Angew. Chem., Int. Ed.*, 2018, **57**, 13283–13287.

33 Z. P. Chen, K. W. Mou, X. H. Wang and L. C. Liu, *Angew. Chem., Int. Ed.*, 2018, **57**, 12790–12794.

34 P. L. Deng, H. M. Wang, R. J. Qi, J. X. Zhu, S. H. Chen, F. Yang, L. Zhou, K. Qi, H. F. Liu and B. Y. Xia, *ACS Catal.*, 2020, **10**, 743–750.

35 Z. Wang, H. F. Su, Y. W. Gong, Q. P Qu, Y. F. Bi, C. H. Tung, D. Sun and L. S. Zheng, *Nat. Commun.*, 2020, **11**, 308–315.

36 D. M. Espinosa, A. L. Rheinggold and T. A. Hanna, *Dalton Trans.*, 2009, **26**, 5226–5238.

37 D. Mansfeld, M. Mehring and M. Schurmann, *Angew. Chem., Int. Ed.*, 2005, **44**, 245–249.

38 E. V. Dikarev, H. T. Zhang and B. Li, *Angew. Chem., Int. Ed.*, 2006, **45**, 5448–5451.

39 Z. Li, Z. H. Lv, H. Yu, Y. Q. Sun, X. X. Li and S. T. Zheng, *CCS Chem.*, 2022, **4**, 2938–2945.

40 M. Mehring, *Coord. Chem. Rev.*, 2007, **251**, 974–1006.

41 L. H. Liu, L. N. Zakharov, A. L. Rheingold and T. A. Hanna, *Chem. Commun.*, 2004, **13**, 1472–1473.

42 D. M. Espinosa and T. A. Hanna, *Dalton Trans.*, 2009, **26**, 5211–5225.

43 L. Jin, X. X. Li, Y. J. Qi, P. P. Niu and S. T. Zheng, *Angew. Chem., Int. Ed.*, 2016, **55**, 13793–13797.

44 J. C. Liu, Q. Han, L. J. Chen, J. W. Zhao, C. Streb and Y. F. Song, *Angew. Chem., Int. Ed.*, 2018, **57**, 8416–8420.

45 S. M. Taylor, S. Sanz, R. D. Mclntosh, C. M. Beavers, S. J. Teat, E. K. Brrchin and S. J. Dalgarno, *Chem.–Eur. J.*, 2012, **18**, 16014–16022.

46 F. Li, G. H. Gu, C. Choi, P. Kolla, S. Hong, T. S. Wu, Y. L. Soo, J. Masa, S. Mukerjee, Y. Jung, J. S. Qiu and Z. Y. Sun, *Appl. Catal., B*, 2020, **277**, 119241–119250.

47 J. W. Shi, S. N. Sun, J. Liu, Q. Niu, L. Z. Dong, Q. Huang, J. J. Liu, R. Wang, Z. F. Xin, D. D. Zhang, J. Y. Niu and Y. Q. Lan, *ACS Catal.*, 2022, **12**, 14436–14444.

48 C. W. Lee, J. S. Hong, K. D. Yang, K. Jin, J. H. Lee, H. Y. Ahn, H. M. Seo, N. E. Sung and K. T. Nam, *ACS Catal.*, 2018, **8**, 931–937.

49 S. S. He, F. L. Ni, Y. J. Ji, L. Wang, Y. Z. Wen, H. P. Bai, G. J. Liu, Y. Zhang, Y. Y. Li, B. Zhang and H. S. Peng, *Angew. Chem., Int. Ed.*, 2018, **130**, 16346–16351.

50 J. J. Liu, N. Li, J. W. Sun, J. Liu, L. Z. Dong, S. J. Yao, L. Zhang, Z. F. Xin, J. W. Shi, J. X. Wang, S. L. Li and Y. Q. Lan, *ACS Catal.*, 2021, **11**, 4510–4519.

51 X. L. Zu, X. D. Li, W. Liu, Y. F. Sun, J. Q. Xu, T. Yao, W. S. Yan, S. Gao, C. M. Wang, S. Q. Wei and Y. Xie, *Adv. Mater.*, 2019, **31**, 1808135.

52 H. C. Hu, H. S. Hu, B. Zhao, P. Cui, P. Cheng and J. Li, *Angew. Chem., Int. Ed.*, 2015, **54**, 11681–11685.

53 P. Cui, H. S. Hu, B. Zhao, J. T. Miller, P. Cheng and J. Li, *Nat. Commun.*, 2015, **6**, 6331–6335.